Supporting Information for:

Sub-picosecond Permittivity of Carbon Nitrides probed with Terahertz Spectroscopy: Revealing high Dielectric Response and Conductivity

Authors:

Reehab Jahangir[1,2,§], Filip Podjaski[1,3,§,*], Paransa Alimard[1], Sam A. J. Hilman[1], Stuart Davidson[2], Stefan Stoica[2], Andreas Kafizas[1], Mira Naftaly[2], James R. Durrant[1,3]

[1]Department of Chemistry and Centre for Processable Electronics, Imperial College London, UK

[2]National Physical Laboratory, Teddington, UK

[3]Department of Chemistry, University of Oxford, UK

[§]equally contributed

*Correspondence to: filip.podjaski@chem.ox.ac.uk

1. Experimental methods:

1.1 Material synthesis and sample preparation:

Graphitic carbon nitride (gC_3N_4) = Melon materials:

g-C_3N_4 #1 (ambient synthesis, 550°C in air, acid/base wash): The material was prepared as reported in literature from a urea precursor, which was dried in an oven at 80°C overnight. 10g of the dried precursor was placed in an alumina crucible and covered with an alumina lid, which was then heated up to 550°C at a heating rate of 5°C/min. It was kept at the maximum temperature for 3 hours, and then cooled down to room temperature. The final product was washed by centrifugation, 3 times each with HCl, NaOH, and finally DI water, respectively. The powder was ground using an agate mortar and pestle. This graphitic carbon nitride is reported to have especially high activity for sacrificial hydrogen evolution (approx. 1 mmol/g/h).[1]

g-C_3N_4 #2 (ambient synthesis, 500°C in air): g-C_3N_4 # 2 was prepared as reported in literature from a urea precursor, which was dried in an oven at 60°C overnight. 30 g of the dried precursor was transferred to an 80 ml alumina crucible with an alumina lid, ensuring the crucible was filled and sealed. The urea was then heated at 500°C for 4 hours in a muffle furnace at a heating rate of 2.5°C/min under an air atmosphere. The final product was left to cool down to room temperature, washed three times with distilled water and ethanol, and dried at 60°C overnight.[2]

g-C_3N_4 #3 (N_2 synthesis, 550°C, CVD oven): g-C_3N_4 # 3 was synthesized by pyrolyzing urea in a nitrogen atmosphere using a reported method with some alterations. Urea was dried overnight at 60°C in an oven. 1.5 g of the dried urea precursor was placed into a 20 ml alumina crucible without a lid. The urea was then heated to 550°C for 4 hours in a CVD furnace with a heating rate of 18°C/min under a nitrogen atmosphere with 2 L/min flow rate. After heating, the product was allowed to cool to room temperature, washed three times with distilled water and ethanol, and dried at 60°C overnight[3].

Porous 2D Carbon Nitrides = Poly(Heptazine Imide) = PHI:

K-PHI #1 (synthesis from melon in Ar atmosphere): K-PHI was synthesized as reported earlier (note: the material was called NCN-Melon first – it was only later resolved that this is K-PHI)[4]. In brief, 800 mg of melon (synthesized from melamine) was ground with 1.6g of dry KSCN and loaded into an aluminium oxide boat into a tube furnace. While keeping a moderate argon flow, the mixture was heated to 400°C at a rate of 30 °C min^{-1}, kept there for 1 h, and then reheated to 500 °C at 30 °C min^{-1} ramp for 30 min. Subsequently, the oven was cooled to room temperature at an unrestricted rate. The resulting yellow mass was suspended in water and the insoluble product was isolated by centrifugation, washed with DI water several times and dried at 60 °C in a vacuum oven.

K-PHI #2: (synthesis from melon in air): g-C_3N_4 # 3 (5 g) was placed in a crucible with a lid and heated at 550°C for three hours (ramp rate 1°C/min) under air. The obtained yellow powder was washed with DI water several times, isolated via centrifugation and ground using a pestle and mortar[5]. This g-C_3N_4 # 3 was used for the synthesis of K-PHI #2 following the same procedure as K-PHI # 2.

H-PHI #1 and #2: 180 mg of the as-synthesised K-PHI (#1 or #2) was stirred overnight at room temperature with 180 ml 1M HCl yielding the protonated product H-PHI. The solution was centrifuged at 8000 rpm for 20 minutes (to concentrate the material and remove the supernatant), and washed with DI water, repeating the process 5-7 times until neutral conditions were reached. The final powder was dried first at 60°C overnight in an oven to remove excess water[6].

Pellets of P3HT (purchased from *Ossila*), melon/g-C_3N_4 and PHI-type carbon nitrides were prepared from their constituent powders, ground finely in an agate mortar and pestle, by pressing about 50-60

mg of the as-synthesised batches using a pressure of approximately 6,000 MPa for 30 seconds in a 10 mm diameter die set in a hydraulic press (Specac Ltd)[7]. The as-prepared pellets are considered as the *ambient* pellets, which correspond to an ambient humidity of 40-60% RH, measured by hygrometers (RS Components) in laboratories. For *dry conditions*, these pellets were kept in a BINDER vacuum oven (<10mbar) at 60 °C overnight. The *wet* pellets were obtained by keeping the material in an airtight box with saturated tissue paper and water (100% relative humidity, monitored with hygrometer) for approximately 4 hours, and measured directly afterwards.

Thin films of K-PHI (used for fs-TAS) were prepared by sonication and stepwise centrifugation of the material[8], and subsequent drop casting of the obtained nanoparticle suspension on plasma-cleaned glass from microscope slides.

1.2 Measurement setups:

THz-TDS: THz-TDS transmission measurements were carried out using a *Teraflash Pro* Time-Domain Terahertz spectrometer Platform from *Toptica Photonics*. In this set up, the THz beam is propagated using 4 parabolic mirrors of 25 mm diameter and 50mm focal length, arranged in a Z-configuration. The samples were placed in the focal plane between mirrors 2 and 3 (see **Figure 1c**) on an iris mount, ensuring it remained in the focal plane and normal to the beam.

UV-VIS: The optical properties have been measured on a Carry 5000 from Agilent, equipped with an integrating sphere, akin to earlier reports [8] . Due to strong scattering of carbon nitride, reflectance data has been used and transformed by Kubelka-Munck analysis into Tauc plots to extract the optical band gap [9]. For the fitting, a direct band gap has been assumed, as reported earlier.

Fs-ns transient pump-push optical absorption spectroscopy (fs-ns TAS): Ultrafast TAS measurements of the thin film CN_x samples were carried out using a commercially available system (Helios, Ultrafast Systems). This system uses a regeneratively amplified Ti:sapphire laser (Solstice, Spectra Physics) which emits 800 nm laser pulses (92 fs, 1 kHz repetition rate). The pump laser pulse (here at 355 nm excitation wavelength) is generated through an optical parametric amplifier (TOPAS Prime, Light Conversion) and a frequency mixer (NirUVis, Light Conversion). The probe pulse measures the sample's absorbance change at specific time delays relative to the pump. Time delays are controlled via a motorised delay stage with adjustable positioning. The probe light used in these experiments is generated by focusing the probe pulse into a sapphire crystal, generating a broad band signal across the visible spectrum. The change in absorbance is recorded in the region between 450-800 nm. The probe pulse is further divided before the sample into two pulses, where one is use as reference to compensate for intensity fluctuations. Both pulses are directed to separated multichannel spectrometer (Si or InGaAs sensor). To acquire pump-probe data, the continuum probe pulse on the samples is spatially overlapped with the pump pulse by maximizing the exciton signal. Every 2nd pump pulse was chopped by a synchronized chopper such that the ground state and excited state of the sample are probed in an alternating manner, and the absorbance difference is calculated from these two signals. Pulse energies were measured using an energy meter (OPHIR Photonics, VEGA P/N 7Z01560), using a 500 µm diameter aperture. To compare humidity conditions, the thin film sample was measured in ambient conditions in an open cuvette. To generate 100% RH, water was added to the bottom of the cuvette, and it was sealed. The sample was remeasured at the same spot after a waiting time of minimum 8h, leaving enough time for equilibration of the atmosphere and the sample with it.

The signal background and the group velocity dispersion were corrected using the software Surface Xplorer 4.2 (Ultrafast Systems). The deconvoluted transient kinetics for the signals tentatively

attributed to excitons (unrelaxed pre-charge signal) and polarons (later charge signal) in our materials were determined using custom-built global analysis software. This software utilises a genetic algorithm in which a defined number of spectral shapes are fit via linear superposition to the experimental data – no physical model is used. In this case, we found that a superposition of two spectra could adequately describe the experimental data, while a third component only reproduces the present two ones, or separates them further spectrally only (not adding value). These spectral shapes can be fixed or freely varying. In this case we used ansatz spectra and allowed their shapes to vary during the fitting, though we note that fixing the ansatz spectra had little effect on the extracted kinetics. We used experimental absorption spectra at > 1ns as the ansatz spectra for the charges, assuming that all unrelaxed or excitonic signals have decayed at times beyond this. The ansatz spectra for the unrelaxed (pre-charge) signal were generated by subtracting the stabilized, reported charge signal in the late ns-regime from initial, sub-ps TAS data containing both signals at the highest fluence data, while confirming the fit all conditions probed.

XRD: X-ray diffraction (XRD) patterns were measured with a Bruker D2 Phaser diffractometer with parallel beam optics equipped with a Lynx-Eye detector. X-rays were generated using a Cu source (V = 30 kV, I = 10 mA) with Cu $K_{\alpha1}$ (λ = 1.54056 Å) and Cu $K_{\alpha2}$ radiation (λ = 1.54439 Å) emitted with an intensity ratio of 2:1. Patterns were collected between $5° \leq 2\theta \leq 60°$ with a step size of 0.02° and time steps of 1 s.

Contact angle measurements: The pellets were gently polished on both sides using wax paper to remove any surface inhomogeneities. An Osilla Contact Angle Goniometer was used to record the contact angle of a 7.5 µl DI water droplet on the surface of the pellet over time. The left-hand side (L.H.S) and right-hand side (R.H.S) contact angle was estimated for each sample at the 30th second using the Manual Points Fitting Procedure on ImageJ, from which the average contact angle is calculated.

Density measurements by Helium Pycnometry: Bulk density of the pellets were determined using a combination of mass measurement and helium pycnometry. Prior to testing the samples were kept in a desiccator and heated additionally to 130°C in a conventional oven to remove excess moisture. The mass of the pellets was determined using a mass comparator and mass standards traceable to the SI unit of mass. The volume of the pellets was determined using helium pycnometry. The sample was placed in sample chamber of know volume (for a 1cm^3 cup, the k=2 uncertainty is 0.0194 g/cm^3) . Helium is introduced to the sample chamber and then expanded into a second empty chamber with a known volume. The pressure observed after filling the sample cell and the pressure discharged into expansion chamber are measured, and from the ration of pressure and chamber volumes the volume of the sample is calculated. Traceability for the measurements is to the SI via the dimensional determination of the volume of a tungsten reference sphere used to calibrate the pycnometer. Density measured by each pycnometer run consists of 10 repeated measurements of the sample under test, referred to as skeletal density, implying that volume of open pores is excluded from the calculation. Since the helium cannot access closed pores, they are included into the total volume and density calculated. Since, even after preconditioning, samples may contain an amount of surface and embedded water it is best practice to perform a few measurements runs, until the results are stable.

2. Supplementary Figures:

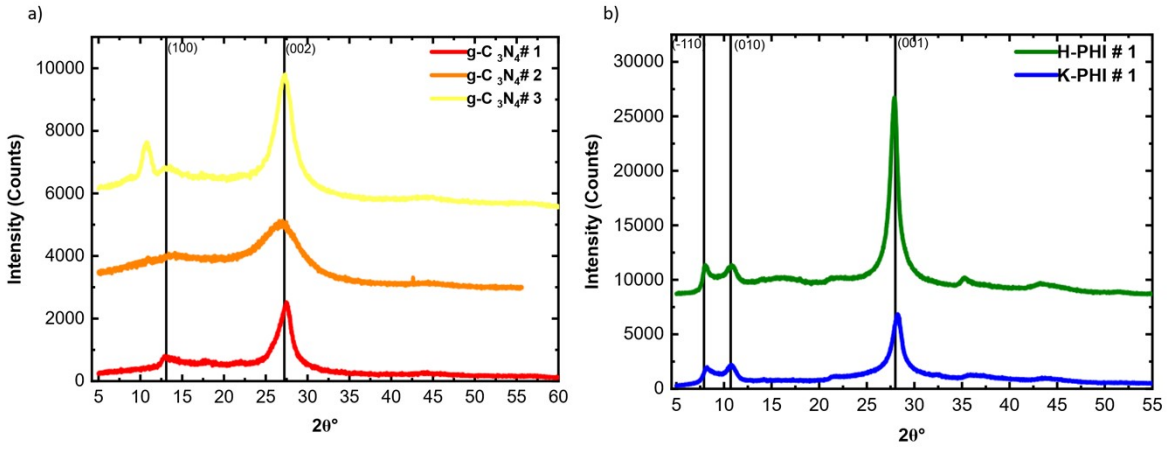

Figure S1: Powder-XRD spectra using Cu-Kα_1 of the carbon nitride materials studied a) graphitic type materials, and b) K- and H-PHI. XRD of PHI batch #2 (earlier reported as NCN-Melon) was reported earlier – the very same batch was used.[10]

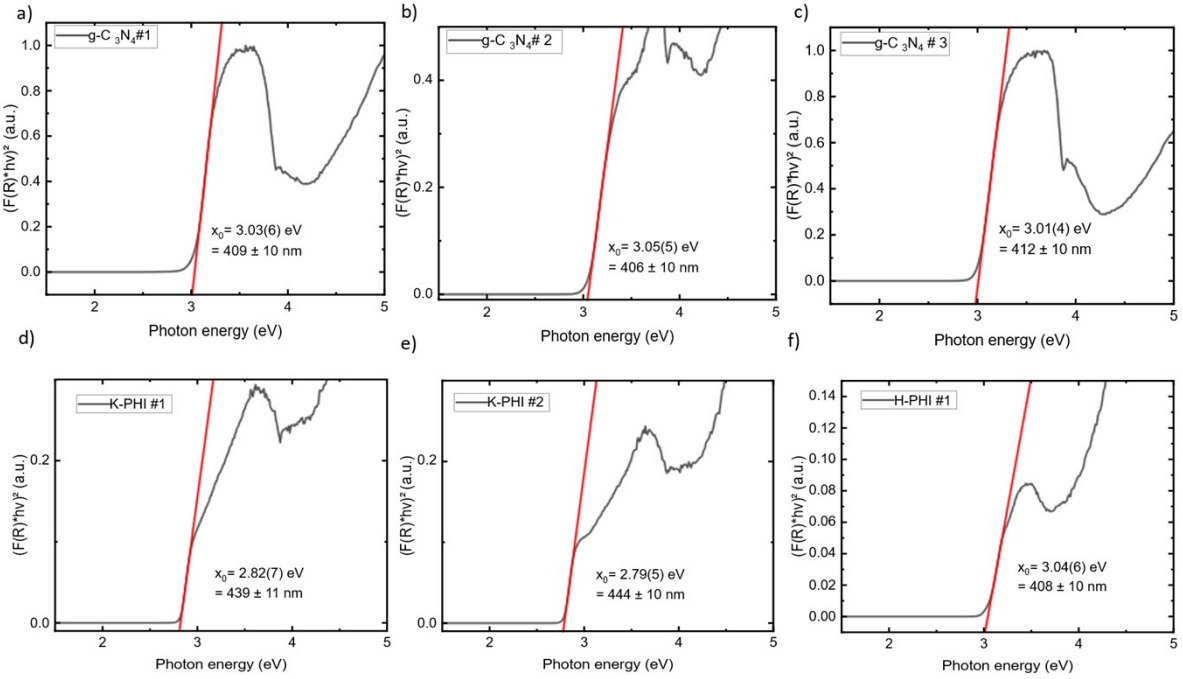

Figure S2: Tauc plots of the CN_x for optical band gap extraction (direct band gap fit) from diffuse reflectance measurements. a) g-C_3N_4 # 1, b) g-C_3N_4 # 2, c) g-C_3N_4 # 3, d) K-PHI #1, e) K-PHI #2, f) H-PHI #1.

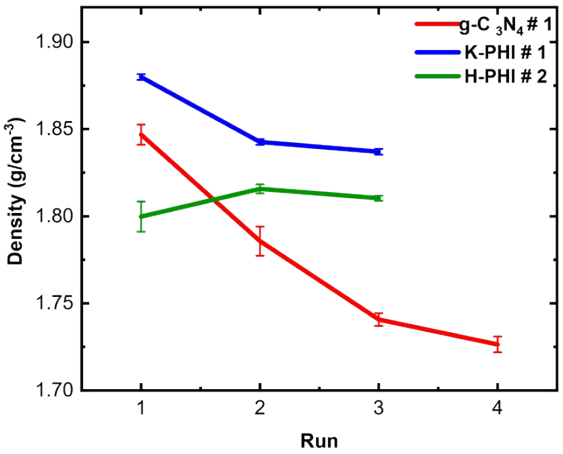

Figure S3: Density measurements by He-Pycnometry: g-C_3N_4 # 1 and K-PHI (#1) kept in ambient conditions initially have a comparable density of 1.85(1) and 1.88(1) g/cm³. H-PHI (#2) has an initial density of 1.80(1) g/cm³. To remove the adsorbed water, the samples were kept in a desiccator and heated additionally to 130°C in a conventional oven for K-PHI until stabilization occurred. The samples considered *dry* have densities of 1.72(1), 1.84(1) and 1.81(1) g/cm³ for g-C_3N_4 , K-PHI and H-PHI, respectively, with error bars representing standard deviation across multiple measurements. These dry densities were assumed for the porosity calculations and have a (k=2) uncertainty value of 0.0194 g/cm³ (see Tables **S1, S2 and S3**).

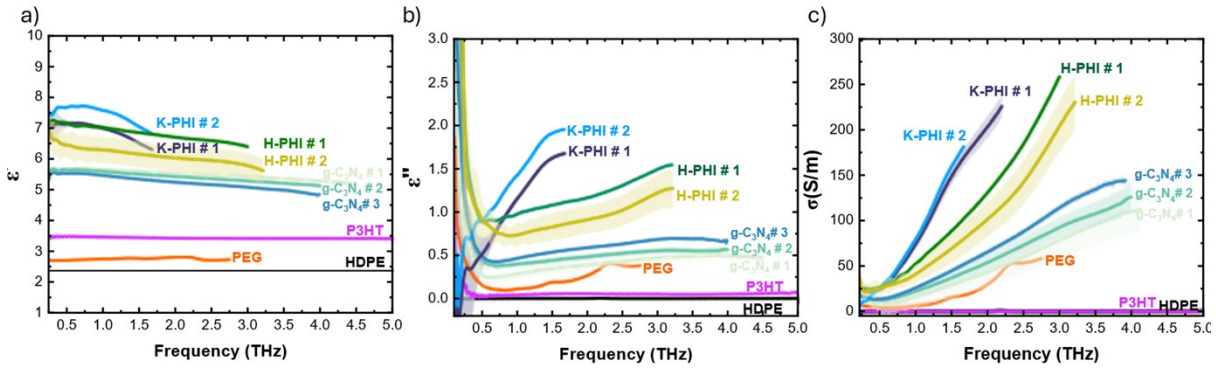

Figure S4: Ambient a) real permittivity ε', b) imaginary permittivity ε'' and c) terahertz conductivity σ for HDPE, PEG, a HDPE reference, PEG (M_w =8,000), the different melon batches (as synthesised in air from urea at 550 °C (g-C_3N_4 # 1), at 500 °C in (g-C_3N_4 # 2), and at 550°C (g-C_3N_4 # 3) in a custom CVD oven under nitrogen flow, and two different batches of K-PHI and H-PHI (protonated from K-PHI batches). The shaded area in the plots indicate the standard deviation measured across 3 pellets of each material.

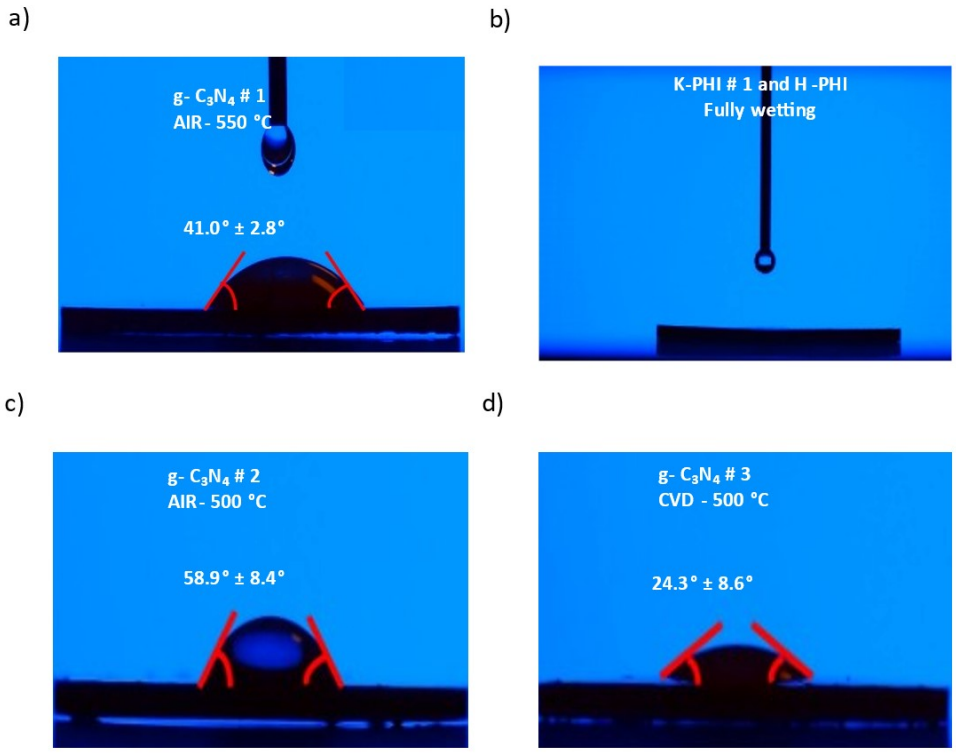

Figure S5: Contact angles of 7.5ul distilled water spherical droplets measured at the 30th second on 10 mm pressed pellets of a) g-C_3N_4 # 1 b) K-PHI # 1 c) g-C_3N_4 # 2 d) g-C_3N_4 # 3. Like K-PHI, H-PHI is also fully wetting. The water droplet is hence not visible any more after 30 s.

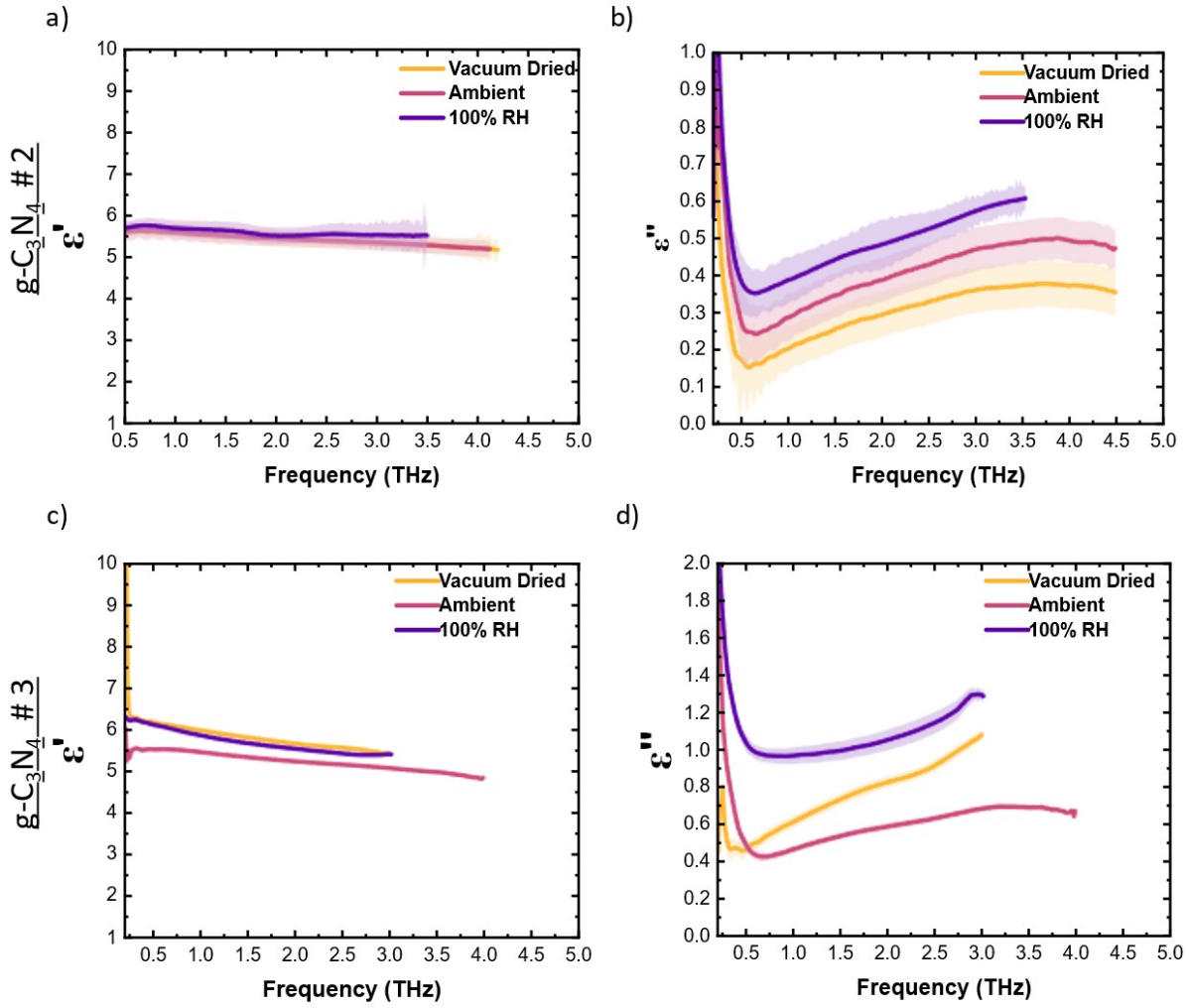

Figure S6: Corresponding humidity dependent real (ε') (**a,c**) and complex permittivity (ε'') (**b,d**) of g-C_3N_4 # 2 and g-C_3N_4 # 3.

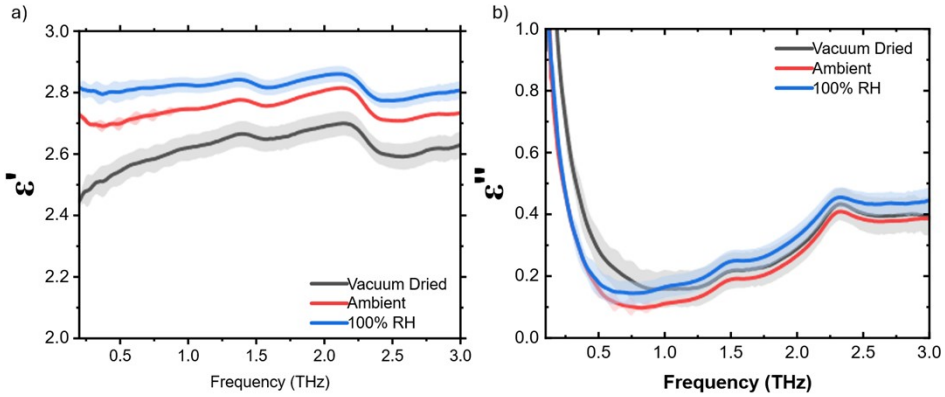

Figure S7: Humidity dependent terahertz complex permittivity of PEG (Mw = 8,000). At 1.5 THz, the ε' values are 2.63 ± 0.05, 2.77 ± 0.01 and 2.82 ± 0.03 for dry, ambient, and wet, respectively, and ones of ε'' are 0.22 ± 0.07, 0.19 ± 0.01 and 0.25 ± 0.04.

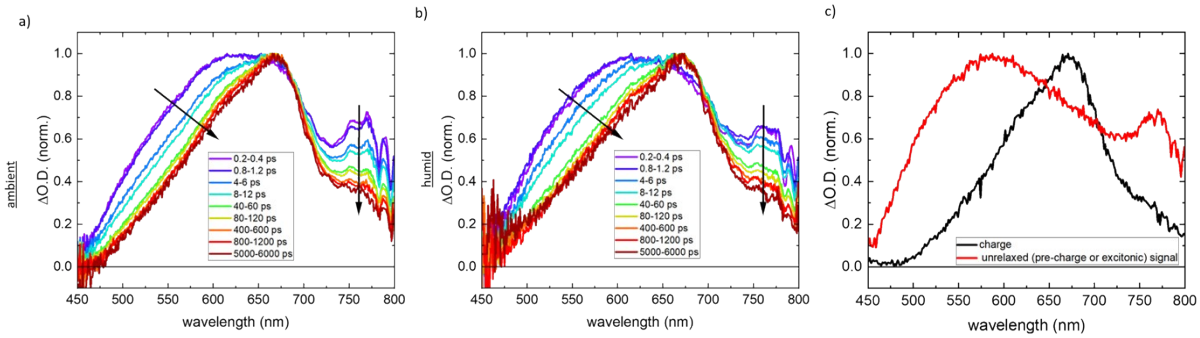

Figure S8: fs-ns transient absorption spectra of K-PHI films in **a)** ambient and **b)** humid conditions (>23 hours in water environment), normalized to the maximum signal at each time (fluence: 250 μJ/cm²). Blue arrows indicate regions where a change in spectral shape is observed, mainly due to a more pronounced, unrelaxed pre-charge signal shoulder in humid conditions, centred at 580 nm (see **Figures S9-S11** for details and raw data). **c)** Deconvoluted spectra of the two signals in K-PHI nanosheets: the relaxed charge signal (black) commonly reported, and the unrelaxed, pre-charge signal feature (red), respectively.

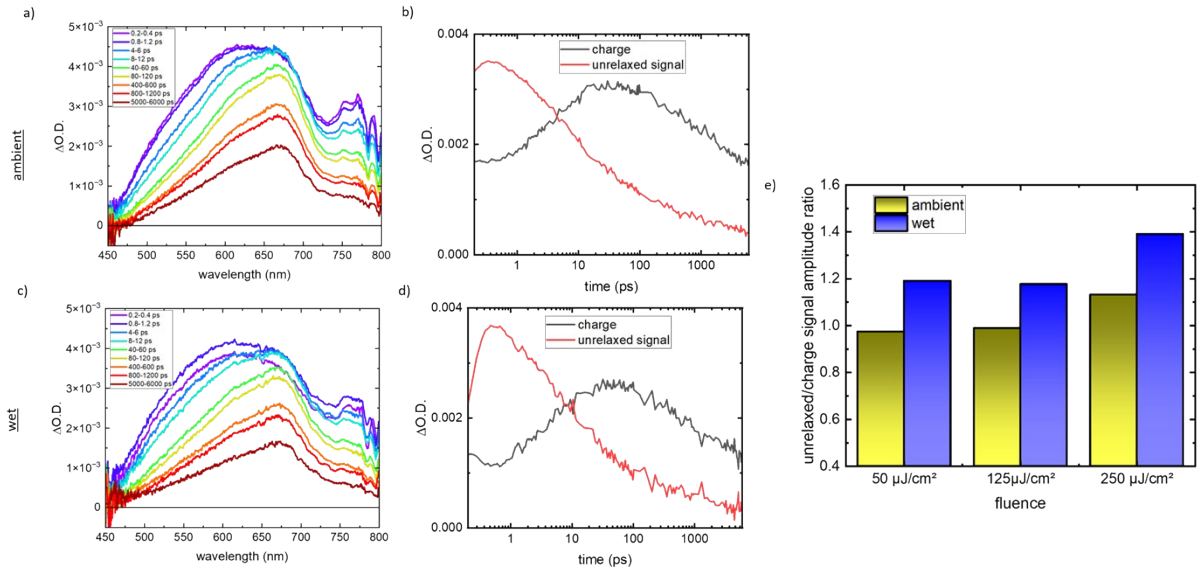

Figure S9: Time-trace of fs-ns transient absorption spectra of K-PHI films in a) ambient and c) wet conditions (same data as in **Fig. S8**). b) & d): Respective time-trace of amplitude of signal attributed to charge, and the one of the unrelaxed (pre-charge) signal, obtained by deconvolution from global analysis. Absolute (unnormalized) signal amplitudes shown here vary from spots. We hence point to the profile of charge and pre-charge species having a stronger rise, and different relative amplitudes in the wet case. e) Comparison of the relative amplitudes of signal strength (normalized to charge signal maximum), for ambient and wet conditions, at different fluences (respective additional raw data shown in **Fig. S10**). In wet conditions, the pre-charge signal feature is consistently more pronounced, indicating its stabilization by increased real permittivity.

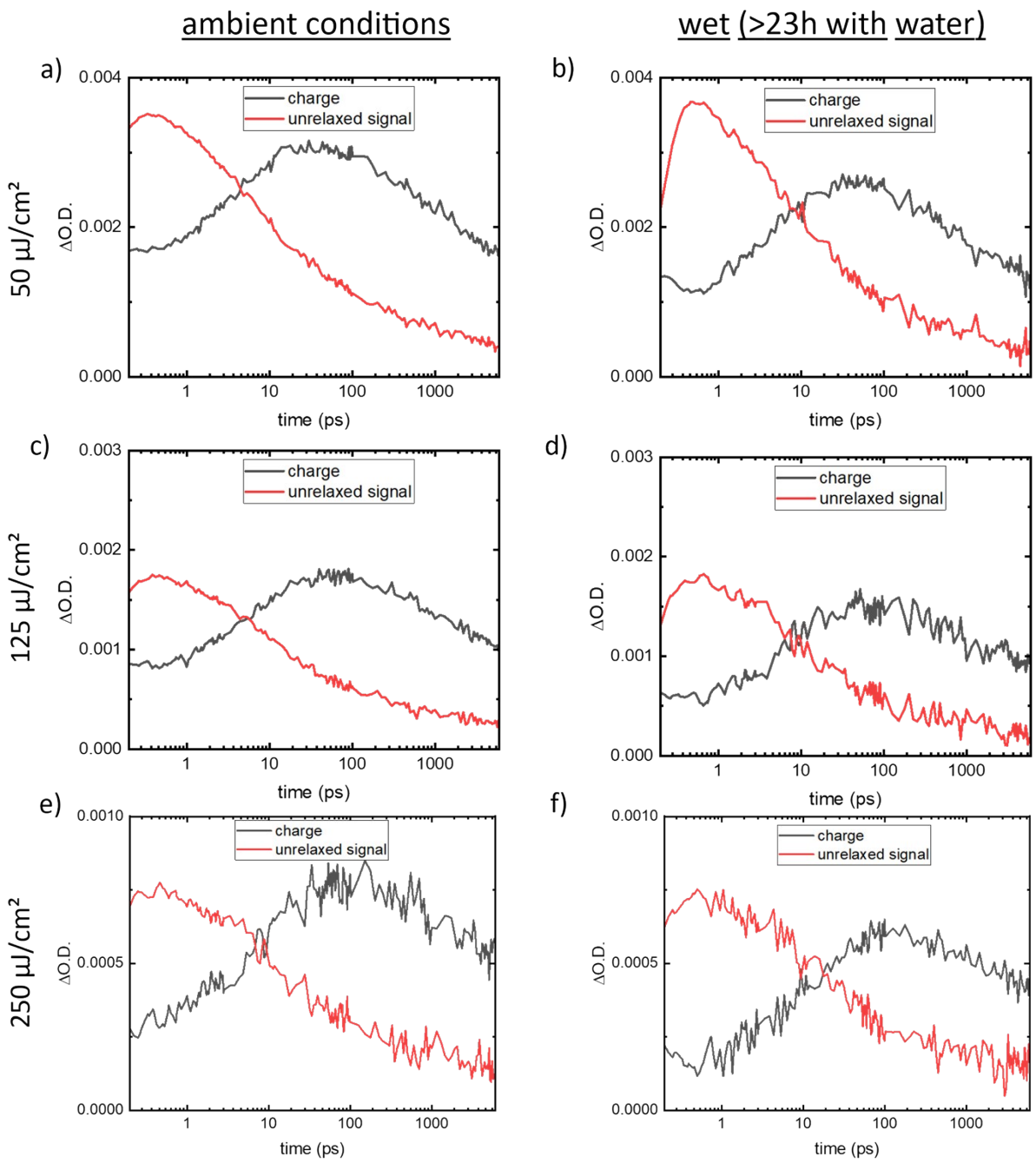

Figure S10: fs-ns transient absorption spectra of K-PHI films in ambient (left) and wet (right) conditions. Traces of charge and unrelaxed (pre-charge) signals after deconvolution as in main text, plotted over time, as function of fluence (top to bottom). The maximum pre-charge signal amplitude increases linearly with fluence in both cases (see **Fig. S11**). Note: Of relevance is only the relative amplitude (ambient vs wet, charge vs unrelaxed signal), and not the absolute amplitude in wet or ambient, which is affected by the measurement spot of not perfectly homogenous samples, and sample swelling with humidity.

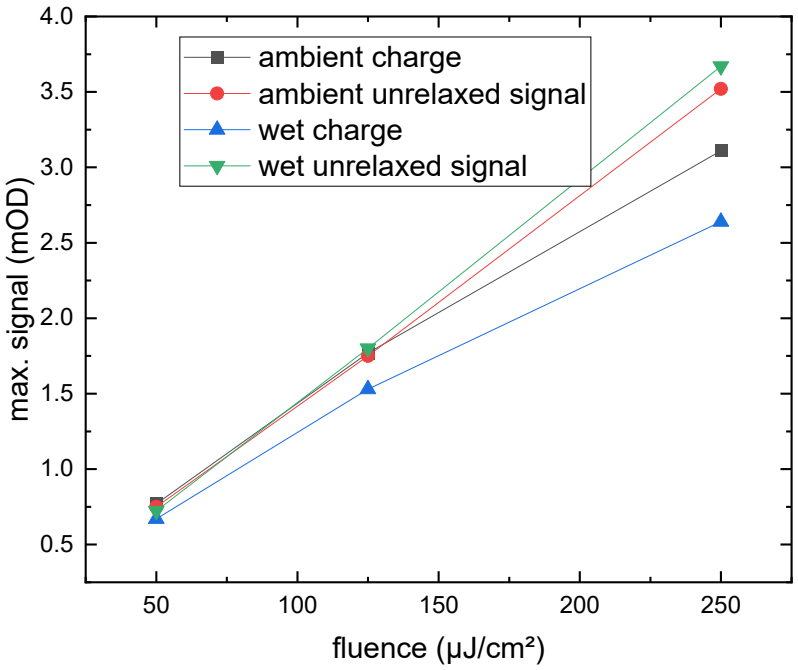

Figure S11: Maximum amplitude of charge and unrelaxed (pre-charge) signal as function of fluence (K-PHI nanoparticles on glass) in the fs-ns-TAS experiments. The early time, unrelaxed signal possibly related to an excitonic feature increases linearly with fluence, thereby excluding bimolecular recombination effects that would artificially modify trends. The second signal, attributed to charges already earlier, appears to be slightly non-linear with increasing laser fluence. Note: Also here, only the degree of linearity is relevant and not absolute amplitudes, which cannot be compared.

3. Supplementary Tables:

Table S1: Average pellet porosity measurements for melon-type CN_x in ambient conditions.

Material	**Density**				
Melon	**1.88 g/cm³**				
Sample	**Mass/ mg**	**Average measured thickness/ mm**	**Optimised Thickness/ mm**	**Approximate Porosity (measured) %**	**Approximate Porosity (optimised) %**
g-C_3N_4 # 1 - 1	57	0.586	0.607	39%	41%
g-C_3N_4 # 1 - 2	50	0.530	0.543	41%	43%
g-C_3N_4 # 1 - 3	55	0.589	0.607	42%	43%
g-C_3N_4 # 2 - 1	49.9	0.446	0.439	30%	29%
g-C_3N_4 # 2 - 2	58.1	0.498	0.484	27%	25%
g-C_3N_4 # 2 - 3	55.6	0.477	0.456	27%	24%
g-C_3N_4 # 3 - 1	54.7	0.523	0.546	35%	38%
g-C_3N_4 # 3 - 2	60.1	0.581	0.609	35%	38%
g-C_3N_4 # 3 - 3	50.8	0.501	0.504	37%	37%

Table S2: average pellet porosity measurements for K-PHI in ambient conditions.

Material	**Density**				
K-PHI	**1.88 g/cm³**				
SAMPLE	**Mass/ mg**	**Average measured thickness/ mm**	**Optimised Thickness/ mm**	**Approximate Porosity (measured) %**	**Approximate Porosity (optimised) %**
K-PHI # 1 - 1	54.1	0.429	0.449	21%	25%
K-PHI # 1 - 2	47.7	0.379	0.399	16%	16%
K-PHI # 1 - 3	60.6	0.485	0.510	21%	25%
K-PHI # 2 - 1	54.3	0.416	0.421	22%	26%
K-PHI # 2 - 2	48	0.374	0.392	23%	25%
K-PHI # 2 - 3	51.1	0.399	0.401	34%	35%

Table S3: average pellet porosity measurements for H-PHI in ambient conditions.

Material	**Density**				
H-PHI	**1.81 g/cm³**				
Sample	**Mass/ mg**	**Average measured thickness/ mm**	**Optimised Thickness/ mm**	**Approximate Porosity (measured) %**	**Approximate Porosity (optimised) %**
H-PHI # 1 - 1	43.6	0.392	0.410	29%	33%
H-PHI # 1 - 2	34.6	0.289	0.298	24%	26%
H-PHI # 1 - 3	35.3	0.302	0.252	9%	11%
H-PHI # 2 – 1	44.2	0.445	0.467	36%	38%
H-PHI # 2 – 2	45.2	0.384	0.403	26%	27%
H-PHI # 2 – 3	45.4	0.365	0.383	22%	23%

Table S4: Summary of porosity corrected ambient THz complex permittivity (**ε**) @ 1.5 THz.

Material	**Real Permittivity ε'** (± 0.04)	**Imaginary Permittivity ε''** (± 0.06)
HDPE	2.39	0.0012
PEG (Mw = 8,000)	2.76	0.19
P3HT	3.44	0.052
g-C_3N_4 # 1 – (550 °C - air)	5.60	0.35
g-C_3N_4 # 2 – (500 °C - air)	5.50	0.44
g-C_3N_4 # 3 – (550 °C – CVD N_2)	5.34	0.54
K-PHI # 1	6.51	1.63
K-PHI # 2	7.05	1.91
H-PHI # 1	6.86	1.06
H-PHI # 2	6.16	0.83

4. Supplementary Notes:

Supplementary Note 1: Porosity corrections for measurement of bulk complex refractive index

The mass and thickness of each pellet was measured using a standard laboratory analytical balance (0.1 mg accuracy) and micrometre screw gauge (0.001 mm) respectively. The estimated average thickness is then used to obtain an optimised thickness value from fitting the data using in-house NPL software, from which an effective pellet density (ρ_{pellet}) is calculated.

The densities of the as-synthesised melon and PHI were characterised with He-pycnometry after drying. These values are used to estimate the porosity *p* of the pellets from the known density of solid material ($\rho_{material}$) using **Equation S1**. The refractive index (***n***) and absorption coefficient α of the solid material were derived from the measured values of porous pellets using the linear mixing model given by **Equations S2** and **S3**.

$$Approximate\ porosity\ p\ = \frac{p_{material} - p_{pellet}}{p_{material}} \quad \text{(Equation S1)}$$

$$n_{pellet} = p + (1 - p)n_{material} \quad \text{(Equation S2)}$$

$$\alpha_{pellet} = p + (1 - p)\alpha_{material} \quad \text{(Equation S3)}$$

The resulting data on the pellets studied are summarized in **Table S1, S2 and S3**. Additionally, the initial and final density measurements for the CN_x materials were used to calculate the approximate porosity of the ambient / 100% RH.[11]

Supplementary Note 2: Acquisition and processing of THz-TDS data

Post detection, the THz signal was Fourier Transformed by the Toptica Photonics TeraFlash Pro software, providing the frequency-dependent field amplitude and phase of the transmitted signal. A reference signal was obtained in the absence of sample in the beam, then signal transmitted through the sample was measured. The refractive index (***n***) and absorption coefficient (α) were extracted from the reference and sample data using **Equations S4** and **S5**. From the absorption coefficient, the extinction coefficient (k), a dimensionless quantity, is calculated according to **Equation S6**. The complex refractive index ***n*** is then given by **Equation S7**.

The information obtained from probing materials with THz waves is well described by Maxwell's wave equations for dielectric media, [12] which gives rise to the complex permittivity (**ε**), related to the complex refractive index (***n***) as per **Equation S8**. The real and imaginary permittivity are calculated using **Equations S9** and **S10** respectively. ε'' can be correlated to THz conductivity σ_{THz} per **Equation S11**.

$$n(\omega) = n_{reference} + (\varphi_{sample} - \varphi_{reference})\frac{c}{\omega d} \quad \text{(Equation S4)}$$

$$\alpha(\omega) = -\frac{2}{d} ln(\frac{(n+1)^2}{4n}\frac{A_{sample}}{A_{reference}}) \quad \text{(Equation S5)}$$

$$a(\omega) = \frac{4\pi f}{c} k(\omega) \quad \text{(Equation S6)}$$

$$n = n + ik \quad \text{(Equation S7)}$$

$$n = \sqrt{\varepsilon_r} \quad \text{(Equation S8)}$$

$$\varepsilon' = n^2(\omega) - k(\omega) \quad \text{(Equation S9)}$$

$$\varepsilon'' = 2n(\omega)k(\omega) \quad \text{(Equation S10)}$$

$$\sigma = \varepsilon''\varepsilon_0\omega \quad \text{(Equation S11)}$$

Supplementary Note 3: Ambient permittivity discussion of polymers

To verify the data acquisition first, a common insulating polymer,High Density Polyethylene (HDPE), was measured as a solid plate. Its measured real permittivity (2.39 ± 0.04, **Figure S4** and **Table S4**) was found to match closely to reported literature (2.37 ± 0.01).[13] A common and highly hygroscopic polymer, poly(ethylene glycol) = PEG, was measured in pellet form with near zero porosity in ambient conditions, with its measured real permittivity at 1.5 THz (2.76 ± 0.04) being larger than that measured at 40-60% relative humidity (RH) at 474 THz using optical waveguide spectroscopy (ε'∼2.09),[14] thus matching expectedure dispersive trends (see **Figure 1a**), and being nearly identical to liquid PEG-400 measured using THz-pulsed spectrometer (ε'∼2.80 and ε'' ~ 0.19 at 1.5 THz).[15]

The dielectric properties of P3HT measured via EIS up to 1 MHz in the 2-electrode set-up have a rather large variability in literature (2.99-3.8)[16–18] due to difficulty in disentangling capacitances arising from dielectric polarisation of the semiconductor layers. Space-charge conduction, solution processing factors such as thickness, homogeneity, solvent variability, casting temperature, concentration of solution used and device architecture all affect measurement of ε' at the lower frequency limit.[17] At 750 THz, ε' measured via SE has been reported as (ε'∼1.24), [19] which altogether tentatively confirms dispersive trends in ε' as well ($\varepsilon'_{1.5\,THz}$ = 3.44). This also further highlights the need to develop accurate and standardised methodology for measuring dielectric properties of organic semiconductors. P3HT has $\sigma_{1.5THz}$ = 4.45 S/m, 3.5x lower than that of PEG, and agrees with D.C conductivity measured using dielectric spectroscopy ($\sigma \sim$ 5-6 S/m). [18]

The porosity-corrected THz complex permittivity spectra for all carbon nitride materials studied are shown in **Figure 2** and the values at 1.5 THz are summarised in **Table S4**. Slight oscillations are observed at frequencies below 1 THz due to the etalon effect, even after data smoothing was applied. All g-C_3N_4_ samples show very similar real permittivity ε', see **Figure S5**, which is approx. 5.5 at 1.5 THz, and significantly higher than our reference materials, and even water (ε'∼4.15). The similarity between melon samples is also observed in the imaginary permittivity spectra (ε'') in **Figure S4b**. All samples show a weak, monotonic and almost linear increase with frequency, which is fairly common in amongst amorphous polymers. [20,21]

The ionic and 2D CN_x K-PHI # 1 and # 2 have been measured over a narrower spectral range of frequencies relative to the melons (**Figure S4a**), due to the steeper rise of their ε" with frequency and limitations imposed by the dynamic range of the system. [22] The average real permittivity (ε') of K-PHI at 1.5 THz is 6.75, which is 22% higher than the average melon value, with the latter having a flatter dispersion profile in its ε' spectra. K-PHI's ε'' at 1.5 THz is approximately 4 times the value of melon (1.77 in average), with a much steeper slope (also characteristic of strong dispersion in ε'). Lastly, H-PHI, where hydrated K^+-pore ions are exchanged for (probably bound) protons, has again a flat ε' dispersion like melon, and ε' = 6.51 in average at 1.5 THz being within error of measurement of H-PHI. The respective ε'' values are ~40% smaller than K-PHI (see **Table S4**) and are twice as high as melon on average, while following a dispersion shape to melon.

Note that the measured frequency range is reduced in moist materials compared with dry ones. This is because absorption increases in the presence of moisture (**Figure 3**), reducing the available frequency range. The maximum measurable absorption is determined by the THz-TDS instrument and falls with frequency following a known relationship. Increased absorption therefore reduces the frequency span of valid measurements. [22]

Supplementary Note 4: THz permittivity comparison of melon samples

At 1.5 THz, g-C_3N_4 # 1 (synthesised at 550 °C and being acid/base washed for improved catalytic activity) has $\varepsilon'_{1.5THz}$ =5.6, which is 0.1 (2%) higher than g-C_3N_4 # 2 (synthesised at 500 °C), possibly due to its higher crystallinity (see **Figure S1**), and by 0.25 (5%) higher than g-C_3N_4 # 3, which may be due to it being less crystalline and hence more defective (**Figure S1**). [3] The relatively high real permittivity of melon at THz frequencies is in agreement with high values of refactive index reported earlier from ellipsometry data, [6 7] and is possibly linked to its chemical structure, which is comprised of cross-linked heptazine units that are expected to be polarizable at THz frequencies and beyond.

Corresponding differences are seen in the imaginary permittivity spectra (ε'') in **Figure S4b**. Within our measurement range from 0.5 to 4 THz, all samples show a weak, monotonic and almost linear increase in ε'', fairly common in amorphous polymers [20]. Trends are the opposite here of those observed for ε', with g-C_3N_4 # 1 having lowest loss factors, and g-C_3N_4 # 2 and g-C_3N_4 # 3 having slightly higher values (+26% and +54% at 1.5 THz, respectively, see **Table 1**). These differences, arising from the different syntheses procedures, are well detectable by THz-TDS and may arise due to different levels of crystallinity, terminal defect types and densities, degree of condensation, or microstructures. This is most apparent when comparing g-C_3N_4 # 1 and # 2, to g-C_3N_4 # 3, where heavy metal contamination is suspected to have occurred from the CVD oven (typically being used for metal oxide synthesis). Such structural defects are possibly giving rise to the extra peak at ~11° in the X-Ray Diffractogram for g-C_3N_4 # 3 (see **Figure S1**).

Supplementary Note 5: Discussion of effects of water uptake

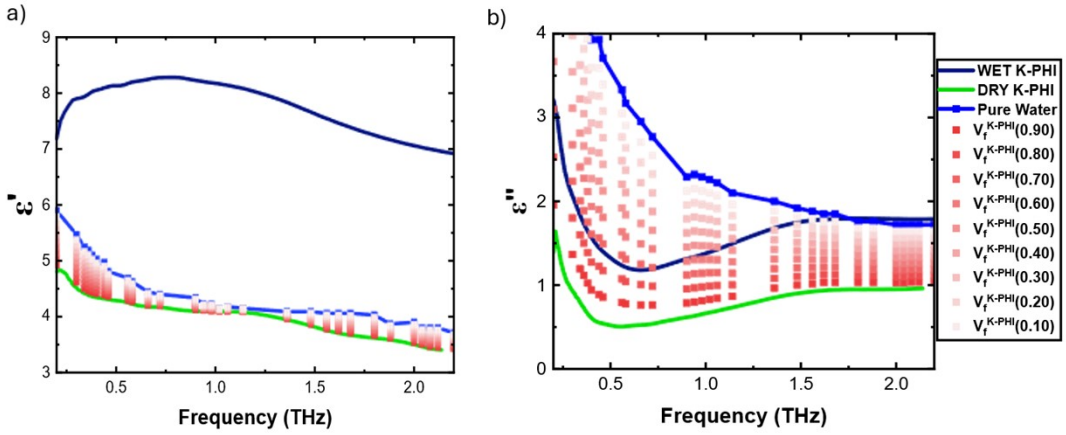

Figure S12: Comparison of complex permittivity spectra (0.1-2.2 THz) between measured K-PHI (wet K-PHI – exposed to high humidity for 4 hours, and DRY K-PHI - vacuum dried for 48 hours at 80 °C), pure water (values extracted and reproduced with permission from [23]) and estimated linear mixes (red data points): **a)** Real permittivity, **b)** imaginary permittivity .

The Terahertz response for wet K-PHI pellets can be compared with that of free water absorption which arises due to activation of stretching and bending modes of the tetrahedral network of water molecules [24]. This is shown in its imaginary permittivity (**Figure S12b**), where pure water has +57% and +28% higher dielectric loss than dried and wetted K-PHI at 1.5 THz, respectively. [9] Real permittivity exhibits an opposing trend, with pure water having similar and approximately 2x lower real permittivity (**Figure S12a**) at 1.5 THz than dried K-PHI and wetted K-PHI, respectively.

To understand how the resultant change in complex permittivity between dried and wet K-PHI arises, a model can be applied treating the samples as a non-interacting mixture of water and dry K-PHI. The spectroscopic properties of a material with multiple components follow the effective medium theory, and by varying the volume fractions V_f of K-PHI and pure water within the sample and applying a linear mixing equation, the effective dielectric properties of a physical mixture of the two species can be calculated, as shown in **Figure S12** between 0.1-0.9 $V_f^{K\text{-}PHI}$ at 0.1 intervals. [25–27]

$$\varepsilon_{sample} = V_f \varepsilon_{(pure\ water)} + V_f \varepsilon_{(dry\ K-PHI)}$$

From **Figure S12a**, as volume fraction of K-PHI ($V_f^{K\text{-}PHI}$) decreases, the estimated dielectric loss of the sample increases. It is seen that the measured real permittivity above 0.5 THz spectrum of wet K-PHI greatly exceeds the estimated permittivity levels for all values of $V_f^{K\text{-}PHI}$. Comparisons in complex permittivity for the different carbon nitride materials can only be made between 0.5 - 5 THz, where both real and imaginary permittivity to exhibit the flat dispersive trend and monotonic, linear increase normally expected in semi-crystalline polymers.

There is a significant coincidence between estimated $V_f^{(K\text{-}PHI)}$ 70 - 80% (0.1 - 1.5 THz) and 10% measured K-PHI (1.5-2.3 THz), which corresponds to ~15-16 mg and ~47 mg of water respectively being absorbed for an average mass of 52 mg per sample. No such significant change in mass in the dried or wet K-PHI pellets was observed on a standard analytical balance, indicating that the change in bound water mass must be below at least 1 mg of the pellet. This, combined with the real permittivity spectra, may lead to the conclusion that the increased permittivity of K-PHI in ambient and humid conditions is an influence of structurally bound, rather than free, water. This hydrophilicity may also arise from the imide bridges forming intermolecular hydrogen bonds (or other terminal defects) [28,29], which further increase the polarizability of the heptazine units that make up K-PHI.

References:

[1] D. J. Martin, K. Qiu, S. A. Shevlin, A. D. Handoko, X. Chen, Z. Guo, J. Tang, *Angew. Chemie* **2014**, *126*, 9394.

[2] X. Wang, Y. Ren, Y. Li, G. Zhang, *Chemosphere* **2022**, *287*, 132098.

[3] D. Wang, H. Zhang, P. Yang, *Colloids Surfaces A Physicochem. Eng. Asp.* **2024**, *689*, 133759.

[4] V. W. Lau, I. Moudrakovski, T. Botari, S. Weinberger, M. B. Mesch, V. Duppel, J. Senker, V. Blum, B. V Lotsch, *Nat. Commun.* **2016**, *7*, 12165.

[5] J. Liu, Y. Liu, N. Liu, Y. Han, X. Zhang, H. Huang, Y. Lifshitz, S.-T. Lee, J. Zhong, Z. Kang, *Science (80-.).* **2015**, *347*, 970.

[6] J. Kröger, F. Podjaski, G. Savasci, I. Moudrakovski, A. Jiménez-Solano, M. W. Terban, S. Bette, V. Duppel, M. Joos, A. Senocrate, R. Dinnebier, C. Ochsenfeld, B. V Lotsch, *Adv. Mater.* **2022**, *34*, e2107061.

[7] K. N. Murphy, M. Naftaly, A. Nordon, D. Markl, *Appl. Sci.* **2022**, *12*, 3475.

[8] F. Podjaski, J. Kröger, B. V Lotsch, *Adv. Mater.* **2018**, *30*, 1705477.

[9] Z. Chen, H. N. Dinh, E. Miller, *Photoelectrochemical Water Splitting*, Springer, New York, **2013**.

[10] H. Kasap, C. A. Caputo, B. C. M. Martindale, R. Godin, V.-H. Lau, B. V Lotsch, J. R. Durrant, E. Reisner, **2016**, *138*, 9183.

[11] M. Naftaly, I. Tikhomirov, P. Hou, D. Markl, *Sensors* **2020**, *20*, 3120.

[12] J. C. Maxwell, *Philos. Trans. R. Soc. London* **1865**, *155*, 459.

[13] M. Naftaly, R. E. Miles, *Proc. IEEE* **2007**, *95*, 1658.

[14] B. Bilen, Y. Skarlatos, G. Aktas, M. N. Inci, T. Dispinar, M. M. Kose, A. Sanyal, *Photonics, Devices, Syst. IV* **2008**, *7138*, 356.

[15] G. R. Musina, A. A. Gavdush, D. K. Tuchina, I. N. Dolganova, G. A. Komandin, S. V Chuchupal, O. A. Smolyanskaya, O. P. Cherkasova, K. I. Zaytsev, V. V Tuchin, in *Saratov Fall Meet. 2018 Opt. Nano-Technologies Biol. Med.*, SPIE, **2019**, pp. 468–476.

[16] M. P. Hughes, K. D. Rosenthal, N. A. Ran, M. Seifrid, G. C. Bazan, T.-Q. Nguyen, *Adv. Funct. Mater.* **2018**, *28*, 1801542.

[17] C. Wang, Z. Zhang, S. Pejić, R. Li, M. Fukuto, L. Zhu, G. Sauvé, *Macromolecules* **2018**, *51*, 9368.

[18] J. Cui, D. E. Martínez-Tong, A. Sanz, T. A. Ezquerra, E. Rebollar, A. Nogales, *Macromolecules* **2016**, *49*, 2709.

[19] L. Hrostea, M. Girtan, R. Mallet, L. Leontie, in *IOP Conf. Ser. Mater. Sci. Eng.*, IOP Publishing, **2018**, p. 12015.

[20] ki Liu, Tsz, *Highlights Sci. Eng. Technol.* **2022**, *15*, 159.

[21] U. Strom, J. R. Hendrickson, R. J. Wagner, P. C. Taylor, *Solid State Commun.* **1974**, *15*, 1871.

[22] P. U. Jepsen, B. M. Fischer, *Opt. Lett.* **2005**, *30*, 29.

[23] W. J. Ellison, *J. Phys. Chem. Ref. data* **2007**, *36*, 1.

[24] H. Zhao, Y. Tan, L. Zhang, R. Zhang, M. Shalaby, C. Zhang, Y. Zhao, X.-C. Zhang, *Light Sci. Appl.*

2020, *9*, 136.

[25] Z. Zang, Z. Li, X. Lu, J. Liang, J. Wang, H.-L. Cui, S. Yan, *Comput. Electron. Agric.* **2021**, *191*, 106515.

[26] M. Bensalem, A. Sommier, J. C. Mindeguia, J. C. Batsale, C. Pradere, *J. Infrared. Millim. Terahertz Waves* **2018**, *39*, 195.

[27] J. F. Federici, *Infrared, Millim. terahertz waves* **2012**, *33*, 97.

[28] J. Kröger, A. Jiménez-Solano, G. Savasci, V. W. h. Lau, V. Duppel, I. Moudrakovski, K. Küster, T. Scholz, A. Gouder, M. Schreiber, *Adv. Funct. Mater.* **2021**, *31*, 2102468.

[29] P. Giusto, D. Cruz, T. Heil, H. Arazoe, P. Lova, T. Aida, D. Comoretto, M. Patrini, M. Antonietti, *Adv. Mater.* **2020**, *32*, e1908140.